www.sciencemag.org/content/347/6224/853/suppl/DC1

Supplementary Materials for

Confining the state of light to a quantum manifold by engineered two-photon loss

Z. Leghtas,* S. Touzard, I. M. Pop, A. Kou, B. Vlastakis, A. Petrenko, K. M. Sliwa, A. Narla, S. Shankar, M. J. Hatridge, M. Reagor, L. Frunzio, R. J. Schoelkopf, M. Mirrahimi, M. H. Devoret

*Corresponding author. E-mail: zaki.leghtas@yale.edu

Published 20 February 2015, *Science* **347**, 853 (2015)
DOI: 10.1126/science.aaa2085

This PDF file includes:

1 Materials and methods

1.1 Qubit fabrication

The transmon qubit was fabricated with a double-angle-evaporated Al/AlO_x/Al Josephson junction, defined using the bridge-free fabrication technique (*30*) on a double-side-polished 2 mm-by-19 mm chip of c-plane sapphire with a 0.43 mm thickness. The aluminum film thickness for each deposition was 20 nm and 30 nm. The Josephson junction has an area of 0.09$\pm$ 0.02 μm^2. Between these two depositions, an AlO_x barrier was grown via thermal oxidation for 6 minutes in 100 Torr static pressure of gaseous mixture 85 % argon 15 % oxygen. The room-temperature junction resistance was 6.67 kΩ.

The sapphire chip was placed across two 3D aluminum cavities separated by a 2 mm wall, as shown in Fig. S2. These cavities were machined out of high purity aluminum (99.99% purity), and prepared by removing $\approx$ 200 μm of material with acid etching (*31*). The antenna pads on each side of the Josephson junction couple to the TE101 mode of each cavity. On the readout cavity side, the antenna is 0.5 mm wide and 7.5 mm long. On the storage cavity side, the antenna is 0.5 mm wide and 4.2 mm long with a 0.01 mm gap capacitor for extra coupling tunability. These dimensions were optimized to meet the desired coupling strengths using finite element simulations and black box circuit quantization analysis (*32*).

1.2 Measurement setup

1.2.1 Waveguide Purcell filter

The output of the readout cavity is coupled to a transmission line through a WR-102 waveguide which exponentially attenuates signals below a cutoff frequency of 5.8 GHz. This way, the readout (7.152 GHz) is above cutoff, and is hence well coupled to the transmission line. On the other hand, the qubit (4.9007 GHz) is below, and is hence isolated from the transmission line. With this architecture, we obtained a qubit lifetime of $T_1 = 23$ μs despite its strong coupling to the low Q readout cavity ($\chi_{qr}/2\pi = 35$ MHz, $\kappa_r = (26 \text{ ns})^{-1}$). Waveguide transmission at the qubit frequency is set by the waveguide length (7.62 cm) and detuning below cutoff, and in our case is -70 dB (at 300 K), while only -0.16 dB (at 300 K) at the cavity frequency. The coupling between the cavity and waveguide is through an aperture, whose dimensions (7.4 mm long, 3.96 mm wide, 5.64 mm deep) determine the coupling strength, which is measured to be Q_r^{out} = 7500 (assuming internal quality factor $Q_r^{\text{in}} \gg Q_r^{\text{out}}$). The input couplings for the readout and storage cavities were measured at room temperature to be Q_r^{in}=4,000,000 and Q_s^{in}=15,000,000. The output port of the storage cavity $Q_s^{\text{out}} \approx Q_s^{\text{in}}$ was not used in this experiment.

1.2.2 Amplification chain

The transmission line is connected to a Josephson parametric converter (JPC) acting as a phase preserving amplifier (*33*), operating near the quantum limit with a gain of 20 dB over a band-

width of 4.6 MHz. We obtain an input noise visibility ratio for the amplification chain of 8 dB, indicating that ≈90% percent of the noise at room temperature are amplified quantum fluctuations. The qubit state is measured by sending a square pulse of length $T_{\text{pulse}} = 1\ \mu$s through the input readout port. The frequency of this pulse is centered at the readout cavity frequency when the qubit is in its ground state. When the qubit is in its ground state $|g\rangle$, the pulse transmits to the cavity output port towards the JPC. Since the dispersive shift is much larger than the cavity line width ($\chi_{qr} \gg \kappa_r \gg 1/T_{\text{pulse}}$), if on the other hand, the qubit is in its excited state $|e\rangle$, the pulse reflects off the input port. When the qubit is in $|g\rangle$, the steady state number of photons in the readout cavity during this pulse is about 4 photons (calibrated using qubit measurement induced dephasing (*34*)).

When exiting the JPC, the pulse propagates through two isolators at 20 mK, a superconducting line between the 20 mK stage and the 4 K stage, where it is amplified by a HEMT amplifier with 40 dB gain. At room temperature, the signal is further amplified, mixed down to 50 MHz and digitized with an analog to digital converter (ADC) (see Fig. S1). For each measurement, we record the two quadratures (I and Q) of the digitized signal. A histogram of 820,000 measured (I,Q) values is shown in Fig. S3. This histogram is the sum of two gaussians: the right one corresponds to the qubit in $|g\rangle$ and the left one corresponds to the qubit in $|e\rangle$ (corresponding to a qubit thermal excited state occupancy of 20%). The I and Q quadratures are rotated such that the information lies in the I quadrature only. The right gaussian is squeezed in the Q quadrature, which is a consequence of the JPC saturation. An (I,Q) value lying on the right (left) hand side of the threshold indicated by dotted line in Fig. S3 is associated to a qubit in the ground (excited) state. This threshold is calculated such that the errors of mistaking $|g\rangle$ for $|e\rangle$ and $|e\rangle$ for $|g\rangle$ are equal. This separability fidelity is calculated here to be 99%, which would coincide with the measurement fidelity in the limit of large T_1.

1.3 System parameters

1.3.1 Parameter values

The system parameters are shown in Tables S1 and S2.

1.3.2 Choice of parameters

As described in the main text, the goal of this experiment was to obtain a non-linear dissipation rate $\kappa_2 = \frac{\chi_{sr}^2}{\kappa_r} |\xi_p|^2$ which is as large as possible. This rate is proportional to the pump power and the square of the readout-storage cross-Kerr χ_{sr}. It is not possible to pump arbitrarily hard since mixing of the pump due to higher order non-linear terms will eventually produce undesirable effects. For example, in Fig. S5, we can see that for pump powers larger than 100 mW (measured at the output of the generator), the storage mode linewidth increases above the linewidth in absence of pump. We have also seen that for pump powers larger than 200 mW, the qubit thermal population starts to increase. This is why we fix the pump power to 100 mW for the rest of the experiment. From the AC Stark shift on the qubit, we know that

this corresponds to $|\xi_p|^2 = 1.2$. Therefore, it is useful to have a large enough χ_{sr} in order to achieve κ_2 of the same order as κ_s for $|\xi_p| \approx 1$. For our parameter values, this corresponds to $\chi_{rs}/2\pi$ of the order of 200 kHz. We designed our system to obtain the latter coupling. We cannot increase this coupling too much since we believe this will decrease the storage cavity lifetime due to the Purcell effect (in the near future, we plan on designing a pass-band, instead of a high-pass, Purcell filter to lift this constraint). Since we have $\chi_{rs} = 2\sqrt{\chi_{rr}\chi_{ss}}$, and we want a storage Kerr at most of the order of its linewidth (in order to minimize the distortion of the coherent state superpositions), we had to increase the readout Kerr χ_{rr} (by increasing the junction participation in this mode (*32*)) until we obtained the desired χ_{rs}. Moreover, we needed to have a qubit mode to perform Wigner tomography. The latter necessitates short un-selective pulses on the qubit (*22*). For this reason, we needed a large enough transmon anharmonicity, which necessarily implied a very large qubit-readout cross-Kerr (here $\chi_{qr}/2\pi = 35$ MHz).

Strongly coupling a qubit to a lossy resonator reduces its coherence times due to the Purcell effect. The use of a Purcell filter (*35*) (described above) seemed favorable. This is why we designed our qubit frequency to be around 5 GHz, and the readout mode around 7 GHz, the former below and the latter above the waveguide cutoff frequency. The pump tone needs to be at $\omega_p = 2\omega_s - \omega_r$, which is below the readout if $\omega_s < \omega_r$ and above otherwise. We thought it would be more cautious to have this strong pump tone as far as possible from the qubit (to avoid the pump coupling to the qubit mode), and therefore designed the storage mode to be about half a GHz above the readout. This way, the pump is one GHz above the readout mode, and hence three GHz above the qubit. The drawback of this design is that the storage mode is not protected by the Purcell filter since it is above cutoff. In the near future we will repeat this experiment with a pass-band Purcell filter.

1.4 Measurement methods

1.4.1 Spectroscopy

Readout mode and qubit spectroscopy are obtained by performing transmission spectroscopy and saturation spectroscopy, respectively. Storage mode spectroscopy is obtained by sequentially sending a long ($100\ \mu s$) and weak probe tone to the storage input port, then performing a selective π pulse (*19*) on the qubit conditioned on there being zero photons in the storage, and finally measuring the qubit through the readout mode. If the probe tone is off-resonant with the storage mode frequency, the storage photon number remains zero, the π pulse therefore inverts the qubit state. On the other hand, if the probe tone is resonant, the storage gets populated to larger photon numbers, hence the π pulse cannot completely invert the qubit state. This change in qubit state vs. probe frequency is detected by the measurement pulse through the readout mode.

1.4.2 Lifetimes

Qubit lifetime T_1 and coherence time T_2 are measured with the usual T_1 and Ramsey pulse sequences. The readout mode lifetime is extracted from its linewidth. Since the readout mode has a relatively large Kerr ($\chi_{rr}/2\pi = 2.14\,\text{MHz}$), the transmission spectra are broadened by this Kerr as we increase the power of the probe tone. Hence, we perform transmission spectroscopy for decreasing probe power until the linewidth stops narrowing. The mode lifetime is then $1/\kappa_r$ where $\kappa_r/2\pi$ is the spectral linewidth at small probe powers. The storage mode lifetime is obtained by first displacing the storage state, and after a variable wait time, measuring the parity of the storage state. By fitting the data, we obtain the storage lifetime.

1.4.3 Thermal population

Qubit thermal population is obtained by taking a single shot histogram of the qubit state (see Fig. S3). We get the thermal excited state occupancy by extracting the probability of getting a count on the left hand side of the threshold (dotted line). We can give a bound on the thermal population n_r^{th} of the readout mode. This thermal population n_r^{th} induces a dephasing rate for the qubit given by $\kappa_{\phi,th} = n_r^{\text{th}}\kappa_r$, in the limit where $\chi_{qr} \gg \kappa_r$ (*36*). We know that the measured dephasing rate $\kappa_\phi = 1/T_2 - 1/2T_1 \approx 1/T_2$ (since $T_1 \gg T_2$), is at least larger than $\kappa_{\phi,th}$. The inequality $\kappa_\phi \geq \kappa_{\phi,th}$ is equivalent to

$$n_r^{\text{th}} \leq 1/(T_2\kappa_r) = 2\% \ .$$

By measuring the qubit number split spectrum to the storage mode, we should in principle be able to measure the storage thermal occupancy. However, the spectrum linewidth sets a bound on which thermal population in the storage one can robustly measure. This linewidth $\kappa_{\text{spec}}/2\pi$ is due to the finite spectroscopy pulse length and power, and is bounded by $(2\pi T_2)^{-1}$. Assuming a small number of thermal photons $n_s^{\text{th}} \ll 1$, at equilibrium, the storage is in a mixture of the vacuum state with probability $(1 - n_s^{\text{th}})$ and the first excited state with probability n_s^{th}. The spectrum of the qubit is then $S(\omega) = (1 - n_s^{\text{th}})S_0(\omega) + n_s^{\text{th}}S_1(\omega)$, where S_0 and S_1 are the qubit spectrums when the number of photons in the storage is 0 or 1, respectively. We have $S_k(\omega) = \frac{\left|\epsilon_{\text{probe}}\right|^2}{\left(\frac{\kappa_{\text{spec}}}{2}\right)^2 + (\omega - \omega_q - k\chi_{qs})^2}$, where ϵ_{probe} is the probe amplitude, and we have neglected the effect of κ_s on κ_{spec} since in practice $\kappa_s \ll \kappa_{\text{spec}}$. When we measured the spectrum S while the storage was in thermal equilibrium, we could not resolve a peak at $\omega_q - \chi_{qs}$ corresponding to one photon. This implies that we have $n_s^{\text{th}}S_1(\omega_q - \chi_{qs}) \leq (1 - n_s^{\text{th}})S_0(\omega_q - \chi_{qs})$. In our case, we took a qubit spectrum with a gaussian π pulse (800 ns standard deviation), and we observed a linewidth κ_{spec}=1/(0.23 μs). In the limit where $\kappa_{\text{spec}} \ll \chi_{qs}$, this sets the following bound on our measure of n_s^{th} :

$$n_s^{\text{th}} \leq (\kappa_{\text{spec}}/2\chi_{qs})^2 = 5\% \ .$$

1.4.4 Cross-Kerr terms

The qubit to readout cross-Kerr is obtained by measuring the readout spectrum. Due to the thermal occupancy of the qubit, this spectrum exhibits two peaks, separated by $\chi_{qr}/2\pi$. The qubit to storage cross-Kerr is obtained by inserting photons in the storage and measuring a qubit spectrum. We see many peaks, each one corresponding to a photon number state in the storage. The linear dependence of the central frequency of each peak on the peak number give the qubit-storage cross-Kerr (see Fig. S4). This measurement is further refined by performing a parity revival experiment (*22*). The readout to storage cross-Kerr is obtained by measuring the readout frequency as a function of photons inserted in the storage. The readout mode frequency decreases linearly with storage photon number with a proportionality constant corresponding to the cross-Kerr.

1.4.5 Kerr terms

The transmon anharmonicity (also termed qubit Kerr χ_{qq}) is obtained by measuring qubit spectroscopy with increasing probe power until we observe the two photon transition from $|g\rangle$ to $|f\rangle$, which is detuned from the main $|g\rangle$ to $|e\rangle$ peak by half the qubit anharmonicity. The readout mode Kerr is obtained from the pump Stark shift (Fig. S5). Indeed, as we will show in the following section, due to the pump, all three modes frequencies decrease linearly with the pump power. The ratio of the slopes of the qubit shift to the readout shift is $\chi_{qr}/2\chi_{rr}$. Hence, knowing χ_{qr}, we extract χ_{rr}. A useful check is to make sure that the ratio of slopes of the qubit and storage shifts is indeed χ_{qr}/χ_{rs}. We find that this value agrees with the independently measured cross-Kerr values with a deviation of 5%. The storage Kerr was not measured, but merely estimated from the formula $\chi_{ss} = \chi_{qs}^2/4\chi_{qq}$ (*32*).

1.4.6 Photon number calibration

The storage cavity was displaced using a 20 ns square pulse. Similarly to (*12*), we calibrate the amplitude of this pulse by measuring a cut of the Wigner function of the vacuum state, and fitting a gaussian to the data. The DAC to photon number correspondence is obtained by imposing that the standard deviation of this gaussian needs to be $1/2$. We calibrate the number of photons in the readout mode by measuring the measurement-induced dephasing rate on the qubit while a tone is applied to the readout mode (*34*).

1.4.7 Phase locking

The quantum state produced in the storage is a consequence of non-linear mixing of the pump and drive tones in our Josephson circuit. If we used a third generator to probe the state of the storage, this generator would not be phase locked to the state in the storage, and hence we would expect all our Wigner functions to be completely smeared and to exhibit no phase coherence. To avoid this problem we generate the pump and storage tones from two separate generators at

respectively ω_p and ω_s, and we mix them at room temperature to generate the drive tone (see dashed box in Fig. S1). This is achieved by doubling the frequency of the storage generator to $2\omega_s$ using a mixer, and then mixing this doubled frequency with the pump to obtain $2\omega_s \pm \omega_p$. The upper sideband at $2\omega_s + \omega_p$ is then filtered by a low pass filter with a 12 GHz cutoff frequency, and hence only the drive tone at the desired frequency $\omega_d = 2\omega_s - \omega_p$ enters our device. We use fast microwave switches controlled by markers from the arbitrary waveform generator (AWG) to produce the pulse sequences for the experiment.

1.4.8 Parity measurement and Wigner tomography

The Wigner function uniquely defines the quantum state ρ_s of an oscillator. It is defined as $W(\alpha) = \frac{2}{\pi}P(\alpha)$, where $P(\alpha) = \text{Tr}\left(\mathbf{D}_{-\alpha}\rho_s\mathbf{D}_\alpha e^{i\pi\mathbf{a}_s^\dagger\mathbf{a}_s}\right)$ (*27, Sec. 6.5*).

In this experiment, we directly measured $P(\alpha = I + iQ)$ following the measurement protocol of (*22, 28*) (see Fig. S6). In the data of Figs. S7-S8, for each point (I_k, Q_k) of the $I - Q$ plane, we repeat 10,000 times:

1. Initialize the qubit by measuring its state and post-selecting on it being in the ground state
2. Displace the cavity state with a 20 ns square pulse of amplitude $a_k = \sqrt{I_k^2 + Q_k^2}$ and phase $\phi_k = \arg(I_k + iQ_k)$
3. Perform a $+\pi/2$ pulse on the qubit around the X-axis.
4. Wait for π/χ_{qs}
5. Perform a $+\pi/2$ pulse on the qubit around the X-axis (then repeat all steps with a $-\pi/2$ pulse)
6. Measure the qubit state

All measurements are single shot and are binned to be 0 or 1 depending on whether the data point lies on the left or right of the threshold (see Fig. S3). Each one of the qubit pulses is a gaussian pulse with a 4 ns standard deviation, and we truncate the pulse length to 5 standard deviations. After post-selecting on the initial measurement, the data is averaged, and two Wigner maps are obtained. One corresponding to both pulses with a $+\pi/2$ angle, and the other where the second pulse is with a $-\pi/2$ angle. We then subtract these two maps in order to correct for systematic errors due to the readout-storage cross-Kerr and the finite un-selectivity of the $\pi/2$ pulses (*22, 28*).

Indeed, assume the storage is in a pure state $|\psi\rangle$, and we want to measure its Wigner function. We model the finite un-selectivity of the $\pi/2$ pulses by assuming that there is an N_{max}, such that if there are $n \leq N_{\text{max}}$ photons in the cavity, the pulses are able to rotate the qubit state, whereas for all $n > N_{\text{max}}$, the qubit state is unaffected by the pulse. Each qubit measurement is thresholded and associated to the qubit being in state g or e. The probability of measuring

$m = g, e$ when the qubit state was in fact in $t = g, e$ is denoted $p^{\alpha}(m|t)$. In the latter notation, the superscript α refers to the displacement amplitude of the storage, which is a simplified model incorporating the readout-storage cross-Kerr and its effect on the readout fidelity due to the presence of photons in the storage. First, we displace the state by α, and denote the displaced state $|\psi_\alpha\rangle$. Second, we perform two $\pi/2$ pulses separated by a π/χ_{qs} wait time. We then obtain the following qubit-storage entangled state :

$$|\psi_\alpha\rangle^{+} = \mathbf{P}_{\text{even}} |\psi_\alpha\rangle |e\rangle + \mathbf{P}_{\text{odd}} |\psi_\alpha\rangle |g\rangle + \mathbf{P}_{>N_{\text{max}}} |\psi_\alpha\rangle |g\rangle \ ,$$

where $\mathbf{P}_{\text{even}} = \sum_{2n \leq N_{\text{max}}} |2n\rangle \langle 2n|$, $\mathbf{P}_{\text{odd}} = \sum_{2n+1 \leq N_{\text{max}}} |2n+1\rangle \langle 2n+1|$ and $\mathbf{P}_{>N_{\text{max}}} = \sum_{n > N_{\text{max}}} |n\rangle \langle n|$. The measured quantity, which is the expectation value of the qubit energy is

$$\begin{aligned} \langle \sigma_z \rangle^{+} &= ||\mathbf{P}_{\text{even}} |\psi_\alpha\rangle||^2 (p^{\alpha}(e|e) - p^{\alpha}(g|e)) - ||\mathbf{P}_{\text{odd}} |\psi_\alpha\rangle||^2 (p^{\alpha}(g|g) - p^{\alpha}(e|g)) \\ &+ ||\mathbf{P}_{>N_{\text{max}}} |\psi_\alpha\rangle||^2 (p^{\alpha}(e|g) - p^{\alpha}(g|g)) \ . \end{aligned}$$

When the second $\pi/2$ pulse has a π phase shift, we get

$$|\psi_\alpha\rangle^{-} = \mathbf{P}_{\text{even}} |\psi_\alpha\rangle |g\rangle + \mathbf{P}_{\text{odd}} |\psi_\alpha\rangle |e\rangle + \mathbf{P}_{>N_{\text{max}}} |\psi_\alpha\rangle |g\rangle \ ,$$

and hence

$$\begin{aligned} \langle \sigma_z \rangle^{-} &= ||\mathbf{P}_{\text{even}} |\psi_\alpha\rangle||^2 (p^{\alpha}(e|g) - p^{\alpha}(g|g)) - ||\mathbf{P}_{\text{odd}} |\psi_\alpha\rangle||^2 (p^{\alpha}(g|e) - p^{\alpha}(e|e)) \\ &+ ||\mathbf{P}_{>N_{\text{max}}} |\psi_\alpha\rangle||^2 (p^{\alpha}(e|g) - p^{\alpha}(g|g)) \ . \end{aligned}$$

We then substract these two expectation values and obtain $\Delta \langle \sigma_z \rangle = C_\alpha (||\mathbf{P}_{\text{even}} |\psi_\alpha\rangle||^2 - ||\mathbf{P}_{\text{odd}} |\psi_\alpha\rangle||^2) = C_\alpha P(\alpha)$, where the contrast C_α is given by $C_\alpha = \frac{1}{2}(p^{\alpha}(g|g) + p^{\alpha}(e|e) - p^{\alpha}(e|g) - p^{\alpha}(g|e))$. In the case of perfect readout: $p^{\alpha}(g|g) = p^{\alpha}(e|e) = 1$ and $p^{\alpha}(e|g) = p^{\alpha}(g|e) = 0$, and hence $C_\alpha = 1$. Notice that this subtraction eliminated the third term in $\langle \sigma_z \rangle^{\pm}$ which is due to the finite un-selectivity of the pulses, and would appear as an offset in the Wigner tomography. This subtraction also makes the effect of the storage-readout cross-Kerr symmetric, making no bias towards positive or negative values.

From these measured Wigner functions, one can reconstruct a density matrix which best reproduces this data (*22*). As a consistency check, we can compare the diagonal elements of this reconstructed density matrix, to the directly measured photon number probabilities using qubit spectroscopy. As shown in Fig. S11, there is a good agreement between these two independent measurements. One can also extract the expectation value of any observable directly from the measured Wigner function, and compare them to the theoretical predictions through numerical simulations. This comparison is made in Figs. S9-S10, and we observe good agreement between theory and experiment.

1.4.9 Qubit dynamics during the pumping

When the pump and the drive tones are on, the readout mode remains mainly in vacuum and the storage state evolves from vacuum to a mixture of coherent states, while transiting through

a coherent state superposition (see Fig. 4 of the main text). In principle, if the Hamiltonian of the three modes (qubit, readout, storage) is fully captured by the Hamiltonian described in Eq. S1Eq. S2, the qubit state should not be influenced by the pumping. For example, if we initialize the qubit in its ground state before activating the pump and drive tones, the qubit should remain in its ground state, unless it absorbs a thermal photon, and this thermal absorption rate should be independent of the number of photons in the two other modes. However, we have observed that when the pumping is on, as the photon number in the storage mode increases, the qubit thermal occupation increases significantly. This is most likely related to the previously unexplained mechanism which causes the qubit lifetime to decrease when photons are inserted in the readout mode (*37*).

The parametric pumping mechanism relies on the frequency matching condition $\omega_p = 2\omega_s - \omega_r$, where $\omega_{p,s,r}$ are the pump, storage and readout frequencies, respectively. The pump and drive tone frequencies need to be tuned with a precision of order g_2, as observed in Fig. 2 of the main paper, and computed in the next section (see Eq. S7). In our experiment, we tune these tones to fulfill this condition when the qubit is in its ground state. If the qubit suddenly jumps to the excited while the pumping is activated, the readout and storage frequencies will shift by their respective dispersive coupling to the qubit χ_{qr} and χ_{qs}. In particular, $(\chi_{qr} - \chi_{qs})/2\pi = 33.4$ MHz $\gg g_2/2\pi = 111$ kHz. Hence, the frequency matching condition no longer holds, and the pumping process is interrupted. This undesirable process can be slightly filtered by measuring the qubit state after completing the pumping, and post-selecting on the qubit being in its ground state (see Fig. S6). However, we do not filter out processes where the qubit jumped up to the excited state for a random time, and jumped back down to its ground state before the measurement is performed. We believe it is these kinds of processes which produce an excess of n=0 population in the storage (see Fig. S11). The effect of these large pumps and populated modes on the qubit decay rates is subject to ongoing research.

2 Supplementary text

2.1 The pumped Josephson circuit Hamiltonian

We start by writing the Hamiltonian of the qubit, readout and storage modes coupled to a Josephson junction, with two tones (the drive and the pump) on the readout mode.

$$\begin{aligned}
\mathbf{H}/\hbar &= \sum_{m=q,r,s} \bar{\omega}_m \mathbf{a}_m^\dagger \mathbf{a}_m - \frac{E_J}{\hbar}\left(\cos(\boldsymbol{\varphi}) + \boldsymbol{\varphi}^2/2\right) + 2\Re\left(\epsilon_p e^{-i\omega_p t} + \epsilon_d e^{-i\omega_d t}\right)\left(\mathbf{a}_r + \mathbf{a}_r^\dagger\right), \\
\boldsymbol{\varphi} &= \sum_{m=q,r,s} \varphi_m(\mathbf{a}_m + \mathbf{a}_m^\dagger) .
\end{aligned}$$

The first term corresponds to the Hamiltonian of three linear modes described by annihilation operator $\mathbf{a}_m$. Their bare frequencies $\bar{\omega}_m$ are shifted towards the measured frequencies ω_m due to the contribution of the Josephson junction in the Hamiltonian. The latter is represented by

the cosine term from which we have removed the quadratic terms by definition of the modes annihilation operators. E_J is the Josephson energy, and $\boldsymbol{\varphi}$ is the phase across the junction, which can be decomposed as the linear combination of the phase across each mode, with φ_m denoting the contribution of mode m to the zero point fluctuations of $\boldsymbol{\varphi}$. The system is irradiated by a drive and pump tones with complex amplitudes $\epsilon_d,\ \epsilon_p$ and frequencies $\omega_d,\ \omega_p$, respectively. $\Re()$ denotes the real part. The pump is a large amplitude far off-resonant tone, while the drive is a weak tone close to resonant with the readout mode.

We place ourselves in a regime where

$$\omega_p,\ \omega_d,\ \bar{\omega}_m \gg \epsilon_p \sim (\omega_p - \bar{\omega}_r) \gg \frac{E_J}{\hbar} \left|\left|\boldsymbol{\varphi}\right|\right|^4/4! \ .$$

In order to eliminate the fastest time scales corresponding to the system frequencies and the pump amplitude, we make a change of frame using the unitary

$$\begin{aligned} U &= e^{i\bar{\omega}_q t \mathbf{a}_q^\dagger \mathbf{a}_q} e^{i\omega_d t \mathbf{a}_r^\dagger \mathbf{a}_r} e^{i\frac{\omega_p+\omega_d}{2} t \mathbf{a}_s^\dagger \mathbf{a}_s} e^{-\tilde{\xi}_p \mathbf{a}_r^\dagger + \tilde{\xi}_p^* \mathbf{a}_r} \ , \\ \frac{d\tilde{\xi}_p}{dt} &= -i\bar{\omega}_r \tilde{\xi}_p - i2\Re\left(\epsilon_p e^{-i\omega_p t}\right) - \frac{\kappa_r}{2}\tilde{\xi}_p \ . \end{aligned}$$

After a time scale of order $1/\kappa_r$ we have $\tilde{\xi}_p \approx \xi_p e^{-i\omega_p t}$, $\xi_p = -i\epsilon_p / \left(\frac{\kappa_r}{2} + i(\bar{\omega}_r - \omega_p)\right) \approx -i\epsilon_p / \left(\frac{\kappa_r}{2} + i(\omega_r - \omega_p)\right)$.

In this new frame, the Hamiltonian is

$$\begin{aligned} \tilde{\mathbf{H}}/\hbar &= (\bar{\omega}_r - \omega_d)\mathbf{a}_r^\dagger \mathbf{a}_r + (\bar{\omega}_s - \frac{\omega_p+\omega_d}{2})\mathbf{a}_s^\dagger \mathbf{a}_s - \frac{E_J}{\hbar}(\cos(\tilde{\boldsymbol{\varphi}}) + \tilde{\boldsymbol{\varphi}}^2/2) \ , \\ \tilde{\boldsymbol{\varphi}} &= \sum_{m=q,r,s} \varphi_m(\tilde{\mathbf{a}}_m + \tilde{\mathbf{a}}_m^\dagger) + (\tilde{\xi}_p + \tilde{\xi}_p^*)\varphi_r \ , \\ \tilde{\mathbf{a}}_q &= e^{-i\bar{\omega}_q t}\mathbf{a}_q \ , \tilde{\mathbf{a}}_r = e^{-i\omega_d t}\mathbf{a}_r \ , \tilde{\mathbf{a}}_s = e^{-i\frac{\omega_p+\omega_d}{2}t}\mathbf{a}_s \ . \end{aligned}$$

We now expand the cosine up to the fourth order, and only keep non-rotating terms:

$$\tilde{\mathbf{H}} \approx \mathbf{H}_{\text{shift}} + \mathbf{H}_{\text{Kerr}} + \mathbf{H}_2 \ , \tag{S1}$$

where :

$$\begin{aligned} \mathbf{H}_{\text{shift}} &= (-\delta_q - \chi_{qr}\left|\xi_p\right|^2)\mathbf{a}_q^\dagger \mathbf{a}_q \\ &+ (\bar{\omega}_r - \omega_d - \delta_r - 2\chi_{rr}\left|\xi_p\right|^2)\mathbf{a}_r^\dagger \mathbf{a}_r \\ &+ (\bar{\omega}_s - \frac{\omega_p+\omega_d}{2} - \delta_s - \chi_{rs}\left|\xi_p\right|^2)\mathbf{a}_s^\dagger \mathbf{a}_s \ , \\ \mathbf{H}_{\text{Kerr}} &= -\sum_{m=q,r,s} \frac{\chi_{mm}}{2}{\mathbf{a}_m^\dagger}^2 \mathbf{a}_m^2 - \chi_{qr}\mathbf{a}_q^\dagger \mathbf{a}_q \mathbf{a}_r^\dagger \mathbf{a}_r - \chi_{qs}\mathbf{a}_q^\dagger \mathbf{a}_q \mathbf{a}_s^\dagger \mathbf{a}_s - \chi_{rs}\mathbf{a}_r^\dagger \mathbf{a}_r \mathbf{a}_s^\dagger \mathbf{a}_s \ , \\ \mathbf{H}_2 &= g_2^* \mathbf{a}_s^2 \mathbf{a}_r^\dagger + g_2 (\mathbf{a}_s^\dagger)^2 \mathbf{a}_r + \epsilon_d \mathbf{a}_r^\dagger + \epsilon_d^* \mathbf{a}_r \ . \end{aligned} \tag{S2}$$

The first term $\mathbf{H}_{\text{shift}}$ corresponds to the modes frequency shifts. The bare frequencies are shifted by $\delta_{q,r,s}$ which arise from the operator ordering chosen in $\mathbf{H}_{\text{Kerr}}$. Moreover, the frequencies are shifted down by a term proportional to $|\xi_p|^2$, which corresponds to the AC Stark shift induced by the pump. We observe this linear shift vs. pump power in Fig. S5.

The second term $\mathbf{H}_{\text{Kerr}}$ corresponds to self-Kerr and cross-Kerr coupling terms (*32*). We have: $\chi_{mm} = \frac{E_J}{\hbar}\varphi_m^4/2$, and $\chi_{mm'} = \frac{E_J}{\hbar}\varphi_m^2\varphi_{m'}^2$.

The last term $\mathbf{H}_2$ contains the terms which reveal the physics we have observed in this paper. It is the microscopic Hamiltonian of a degenerate parametric oscillator (*9*). The first term in this Hamiltonian is a non-linear coupling between the storage and readout modes: two photons from the storage can swap with a single photon in the readout. In contrast to the usual parametric oscillator, our readout mode is not twice the frequency of the storage mode. This term is produced by four-wave mixing of the pump and the readout and storage modes. The term in ϵ_d corresponds to a drive on the readout mode. Our coupling strength is given by

$$g_2 = \chi_{sr}\xi_p^*/2 \ .$$

The second term in $\mathbf{H}_2$ is a coherent drive on the readout mode. It corresponds to the input energy which is converted into pairs of photons in the storage, thus creating coherent state superpositions.

2.2 Two-mode model and semi-classical analysis

Here we assume the qubit remains in its ground state. The storage and readout modes evolve under the Hamiltonian:

$$\begin{aligned}
\mathbf{H}_{sr} &= \Delta_d \mathbf{a}_r^\dagger \mathbf{a}_r + \frac{\Delta_p + \Delta_d}{2}\mathbf{a}_s^\dagger \mathbf{a}_s \\
&+ g_2^* \mathbf{a}_s^2 \mathbf{a}_r^\dagger + g_2 (\mathbf{a}_s^\dagger)^2 \mathbf{a}_r + \epsilon_d \mathbf{a}_r^\dagger + \epsilon_d^* \mathbf{a}_r \qquad \text{(S3)} \\
&- \chi_{rs}\mathbf{a}_r^\dagger \mathbf{a}_r \mathbf{a}_s^\dagger \mathbf{a}_s - \sum_{m=r,s} \frac{\chi_{mm}}{2} {\mathbf{a}_m^\dagger}^2 \mathbf{a}_m^2 \ , \qquad \text{(S4)}
\end{aligned}$$

where $\Delta_d = \bar{\omega}_r - \omega_d - \delta_r - 2\chi_{rr}|\xi_p|^2$ and $\Delta_p = -\Delta_d + 2(\bar{\omega}_s - \frac{\omega_p+\omega_d}{2} - \delta_s - \chi_{rs}|\xi_p|^2)$. Theory curves of Fig.2 in the main paper are obtained by numerically finding the steady state density matrix of the Lindblad equation with damping operators $\sqrt{\kappa_r}\mathbf{a}_r$ and $\sqrt{\kappa_s}\mathbf{a}_s$ and Hamiltonian $\mathbf{H}_{sr}$.

We now write the quantum Langevin equations with damping, which require including incoming bath fields $\mathbf{a}_r^{in}$ and $\mathbf{a}_s^{in}$ (*14, Sec. 4.4*):

$$\begin{aligned}
\frac{d}{dt}\mathbf{a}_r &= -i[\mathbf{a}_r, \mathbf{H}_{sr}] - \frac{\kappa_r}{2}\mathbf{a}_r + \sqrt{\kappa_r}\mathbf{a}_r^{in} \ , \\
\frac{d}{dt}\mathbf{a}_s &= -i[\mathbf{a}_s, \mathbf{H}_{sr}] - \frac{\kappa_s}{2}\mathbf{a}_s + \sqrt{\kappa_s}\mathbf{a}_s^{in} \ .
\end{aligned}$$

The remainder of this section is devoted to gaining some insight into the steady state solutions of the equations above. We simplify this task by neglecting the Kerr terms in the Hamiltonian. This leads us to:

$$\frac{d}{dt}\mathbf{a}_r = -i\Delta_d\mathbf{a}_r - ig_2^*\mathbf{a}_s^2 - i\epsilon_d - \frac{\kappa_r}{2}\mathbf{a}_r + \sqrt{\kappa_r}\mathbf{a}_r^{in} \ , \tag{S5}$$

$$\frac{d}{dt}\mathbf{a}_s = -i\frac{\Delta_p+\Delta_d}{2}\mathbf{a}_s - 2ig_2\mathbf{a}_s^\dagger\mathbf{a}_r - \frac{\kappa_s}{2}\mathbf{a}_s + \sqrt{\kappa_s}\mathbf{a}_s^{in} \ . \tag{S6}$$

We can further simplify these nonlinear Langevin equations by taking the classical limit, where the field operators are replaced by their complex expectation values (*14, Sec. 4.4*):

$$\begin{aligned} 0 &= -i\Delta_d a_r - ig_2^* a_s^2 - i\epsilon_d - \frac{\kappa_r}{2}a_r \ , \\ 0 &= -i\frac{\Delta_p+\Delta_d}{2}a_s - 2ig_2 a_s^* a_r - \frac{\kappa_s}{2}a_s \ . \end{aligned}$$

One solution is

$$a_s = 0 \ , a_r = -i\epsilon_d/(\frac{\kappa_r}{2} + i\Delta_d) \ . \tag{S7}$$

This is the usual classical Lorentzian response of a driven-damped oscillator. Now assuming $a_s \neq 0$, we obtain a second solution for a_r:

$$a_r = \frac{-\Delta_p - \Delta_d + i\kappa_s}{4g_2}e^{2i\theta_s} \ ,$$

where θ_s is the phase of a_s. Here, the modulus squared of a_r is a parabolic function of the detuning $\Delta_p + \Delta_d$ with a width of $1/\left|4g_2\right|^2$, and a minimal value $\left|\kappa_s/4g_2\right|^2$. This corresponds to the dip observed in Fig. 2 of the main paper, and its depth is a direct signature of the fact that $g_2 \gg \kappa_s$. The response of the storage cavity a_s verifies:

$$\begin{aligned} a_s^2 &= \frac{1}{g_2^*}(-\Delta_d + i\frac{\kappa_r}{2})a_r - \frac{\epsilon_d}{g_2^*} \ , \\ \left|a_s\right|^2 &= \frac{1}{4\left|g_2\right|^2}(\Delta_d - i\frac{\kappa_r}{2})(\Delta_p + \Delta_d - i\kappa_s) - \frac{\epsilon_d}{g_2^*}e^{-2i\theta_s} \ . \end{aligned}$$

A sufficient condition for this equation to have a solution is

$$\frac{\left|\Delta_d - i\frac{\kappa_r}{2}\right|\left|\Delta_p + \Delta_d - i\kappa_s\right|}{4\left|g_2\epsilon_d\right|} \leq 1 \ .$$

A model for the response $\left|a_r\right|^2$ of the readout mode as a function of the readout probe and pump tone detunings is:

$$\left|a_r\right|^2(\Delta_r, \Delta_p) = \min\left(\frac{\left|\epsilon_d\right|^2}{\frac{\kappa_r^2}{4} + \Delta_d^2}, \frac{(\Delta_p+\Delta_d)^2 + \kappa_s^2}{16\left|g_2\right|^2}\right) \ .$$

We have checked that this simple semi-classical expression without Kerr terms captures the main features of the data in Fig. 2 (a) of the main paper. However, the transient coherent state superposition shown in Fig. 4 of the main paper cannot be explained by such a semi-classical model: it is a quantum signature of our system.

2.3 Single-mode model and classical analysis

2.3.1 Adiabatic elimination of the readout mode

We can adiabatically eliminate the readout mode (*18, Sec. 12.1*), and obtain a master equation for the reduced density matrix of the storage mode alone. Let ρ_{sr} be the density matrix which represents the joint readout and storage state. It verifies

$$\frac{d}{dt}\rho_{sr} = -i[\mathbf{H}_{sr}, \rho_{sr}] + \frac{\kappa_r}{2}\mathbf{D}[\mathbf{a}_r]\rho_{sr} + \frac{\kappa_s}{2}\mathbf{D}[\mathbf{a}_s]\rho_{sr} \ , \tag{S8}$$

where the Hamiltonian $\mathbf{H}_{sr}$ is given in Eq. S4, and here we take $\Delta_d = \Delta_p = 0$. Let δ be a small dimensionless parameter $\delta \ll 1$. We place ourselves in the regime where $g_2/\kappa_r, \epsilon_d/\kappa_r, \chi_{rs}/\kappa_r \sim \delta$ and $\chi_{ss}/\kappa_r, \kappa_s/\kappa_r \sim \delta^2$. We assume that the number of photons in the readout mode is always much smaller than one. We then search for a solution of Eq. S8 in the form

$$\rho_{sr} = \rho_{00}\left|0\right\rangle\left\langle 0\right| + \delta\left(\rho_{01}\left|0\right\rangle\left\langle 1\right| + \rho_{10}\left|1\right\rangle\left\langle 0\right|\right) + \delta^2\left(\rho_{11}\left|1\right\rangle\left\langle 1\right| + \rho_{02}\left|0\right\rangle\left\langle 2\right| + \rho_{20}\left|2\right\rangle\left\langle 0\right|\right) + O(\delta^3) \ ,$$

where ρ_{mn} acts on the storage Hilbert space, whereas $\left|m\right\rangle\left\langle n\right|$ act on the readout Hilbert space. The goal here is to derive the dynamics of $\rho_s = \mathrm{Tr}_r(\rho_{sr}) = \rho_{00} + \delta^2\rho_{11}$ up to second order in δ, where Tr_r denotes the partial trace over the readout degrees of freedom. First, lets multiply Eq. S8 by $\langle 0|$ and $|0\rangle$. We get, up to second order terms in δ :

$$\begin{aligned}
\frac{d}{\kappa_r dt}\rho_{00} &= -\frac{i}{\kappa_r}\left\langle 0\right|\left[\mathbf{H}_{sr}, \rho\right]\left|0\right\rangle + \delta^2\rho_{11} + \frac{\kappa_s}{2\kappa_r}\mathbf{D}[\mathbf{a}_s]\rho_{00} + O(\delta^3) \\
&= -i\delta^2\left(\mathbf{A}^\dagger\rho_{10} - \rho_{01}\mathbf{A}\right) - i[-\frac{\chi_{ss}}{2\kappa_r}(\mathbf{a}_s^\dagger)^2\mathbf{a}_s^2, \rho_{00}] + \delta^2\rho_{11} + \frac{\kappa_s}{2\kappa_r}\mathbf{D}[\mathbf{a}_s]\rho_{00} \\
&+ O(\delta^3) \ ,
\end{aligned} \tag{S9}$$

where $\mathbf{A} = \frac{1}{\delta\kappa_r}(g_2^*\mathbf{a}_s^2 + \epsilon_d)$, and hence $||A|| = O(1)$ in δ. We now need to find expressions of $\rho_{01,10,11}$ up to 0^{th} order terms in δ. We find, neglecting terms of order δ and higher:

$$\frac{d}{\kappa_r dt}\rho_{10} = -i\mathbf{A}\rho_{00} - \frac{1}{2}\rho_{10} + O(\delta) \ , \tag{S10}$$

$$\frac{d}{\kappa_r dt}\rho_{11} = -i\left(\mathbf{A}\rho_{01} - \rho_{10}\mathbf{A}^\dagger\right) - \rho_{11} + O(\delta) \ . \tag{S11}$$

The derivative of ρ_{10} has two terms: the first one can be interpreted as an external driving term, and the second is a damping term. Although the first term is time dependent, making this

equation difficult to solve exactly, we know that its temporal variation is slow (of order δ^2) in comparison to the damping rate (of order 1). This is where we make the adiabatic approximation: we assume that ρ_{10} is continuously in its steady state. The same reasoning then applies to ρ_{11}, which yields:

$$\begin{aligned}
\rho_{10} &= -2i\mathbf{A}\rho_{00} + O(\delta) \ , && \text{(S12)}\\
\rho_{11} &= -i\left(\mathbf{A}\rho_{01} - \rho_{10}\mathbf{A}^\dagger\right) + O(\delta) && \text{(S13)}\\
&= 4\mathbf{A}\rho_{00}\mathbf{A}^\dagger + O(\delta) \ . && \text{(S14)}
\end{aligned}$$

Injecting these expressions in Eq. S9, and rearranging terms, we find

$$\begin{aligned}
\frac{d}{dt}\rho_s &= -i[\mathbf{H}_s, \rho_s] + \frac{\kappa_2}{2}D[\mathbf{a}_s^2]\rho_s + \frac{\kappa_s}{2}D[\mathbf{a}_s]\rho_s \ ,\\
\mathbf{H}_s &= \epsilon_2^*\mathbf{a}_s^2 + \epsilon_2(\mathbf{a}_s^\dagger)^2 - \frac{\chi_{ss}}{2}\mathbf{a}_s^{\dagger 2}\mathbf{a}_s^2 \ ,
\end{aligned}$$

with

$$\kappa_2 = 4\left|g_2\right|^2/\kappa_r \ , \qquad \epsilon_2 = -2ig_2\epsilon_d/\kappa_r \ .$$

This result can be found in (*18, Eq. 12.10*), where the modes have no Kerr and cross-Kerr couplings.

2.3.2 Semi-classical analysis

Let us define $\alpha(t) = \mathrm{Tr}\left(\mathbf{a}_s\rho_s\right)$ and calculate its dynamics. Using $[\mathbf{a}_s, (\mathbf{a}_s^\dagger)^2] = 2\mathbf{a}_s^\dagger$, $[\mathbf{a}_s, \mathbf{a}_s^{\dagger 2}\mathbf{a}_s^2] = 2\mathbf{a}_s^\dagger\mathbf{a}_s^2$ and $\mathrm{Tr}\left(\mathbf{a}_s D[\mathbf{a}_s^2]\rho_s\right) = -2\mathrm{Tr}\left(\mathbf{a}_s^\dagger\mathbf{a}_s^2\rho_s\right)$, we find

$$\frac{d}{dt}\alpha = -2i\epsilon_2\mathrm{Tr}\left(\mathbf{a}_s^\dagger\rho_s\right) + i\chi_{ss}\mathrm{Tr}\left(\mathbf{a}_s^\dagger\mathbf{a}_s^2\rho_s\right) - \kappa_2\mathrm{Tr}\left(\mathbf{a}_s^\dagger\mathbf{a}_s^2\rho_s\right) - \frac{\kappa_s}{2}\alpha \ .$$

Let us assume a solution in the form of a coherent state $\rho_s(t) = |\alpha(t)\rangle\langle\alpha(t)|$, we then find

$$\frac{d}{dt}\alpha = -2i\epsilon_2\alpha^* - \left(-i\chi_{ss} + \kappa_2\right)|\alpha|^2\alpha - \frac{\kappa_s}{2}\alpha \ .$$

The central panel of Fig. 3 of the main paper illustrates this equation. The white lines correspond to trajectories governed by this equation, and the absolute value $\left|\frac{d}{dt}\alpha\right|$ is represented by the colormap.

In steady state $\alpha(t) \to \alpha_\infty$, and we have

$$0 = -2i\epsilon_2\alpha_\infty^* - \left(-i\chi_{ss} + \kappa_2\right)|\alpha_\infty|^2\alpha_\infty - \frac{\kappa_s}{2}\alpha_\infty \ .$$

We write α_∞ in the form $\alpha_\infty = r_\infty e^{i\theta_\infty}$ and $-i\chi_{ss} + \kappa_2 = r_2 e^{i\varphi_2}$:

$$2i\epsilon_2 r_\infty e^{-i\theta_\infty} = -r_2 e^{i\varphi_2} r_\infty^2 r_\infty e^{i\theta_\infty} - \frac{\kappa_s}{2} r_\infty e^{i\theta_\infty} .$$

Notice that $\alpha_\infty = 0$ is a solution, now assume $\alpha_\infty \neq 0$:

$$-2i\epsilon_2 e^{-2i\theta_\infty} = r_2 e^{i\varphi_2} r_\infty^2 + \frac{\kappa_s}{2} .$$

Taking the module square of this equation we get

$$r_2^2 r_\infty^4 + r_2 \kappa_s \cos(\varphi_2) r_\infty^2 + \frac{\kappa_s^2}{4} - 4\left|\epsilon_2\right|^2 = 0 .$$

The latter equation is quadratic in r_∞^2, and we assume φ_2 small enough in order for its discriminant to be positive. If $|\epsilon_2| \leq \frac{\kappa_s}{4}$, this equation has no positive roots and hence $\alpha_\infty = 0$ is the unique solution.

Now lets assume $|\epsilon_2| > \frac{\kappa_s}{4}$, then

$$r_\infty^2 = \frac{1}{2r_2^2}\left(-r_2\kappa_s\cos(\varphi_2) + \sqrt{\left(r_2\kappa_s\cos(\varphi_2)\right)^2 - 4r_2^2(\frac{\kappa_s^2}{4} - 4\left|\epsilon_2\right|^2)}\right) ,$$

and two solutions exist for the phase θ_∞:

$$\begin{aligned} \theta_\infty^- &= \theta_2/2 + 3\pi/4 - \varphi_K/2 \\ \theta_\infty^+ &= \theta_\infty^- + \pi , \end{aligned}$$

where θ_2 is the phase of ϵ_2, and $\varphi_K = \arctan(\frac{r_\infty^2 r_2 \sin(\varphi_2)}{r_\infty^2 r_2 \cos(\varphi_2) + \kappa_s/2})$

Note that if $\chi_{ss} = 0$, then $r_2 = \kappa_2$ and $\varphi_2 = 0$ and we find

$$r_\infty\Big|_{\chi_{ss}=0} = \sqrt{\frac{2\left|\epsilon_2\right| - \kappa_s/2}{\kappa_2}} .$$

3 Supplementary figures

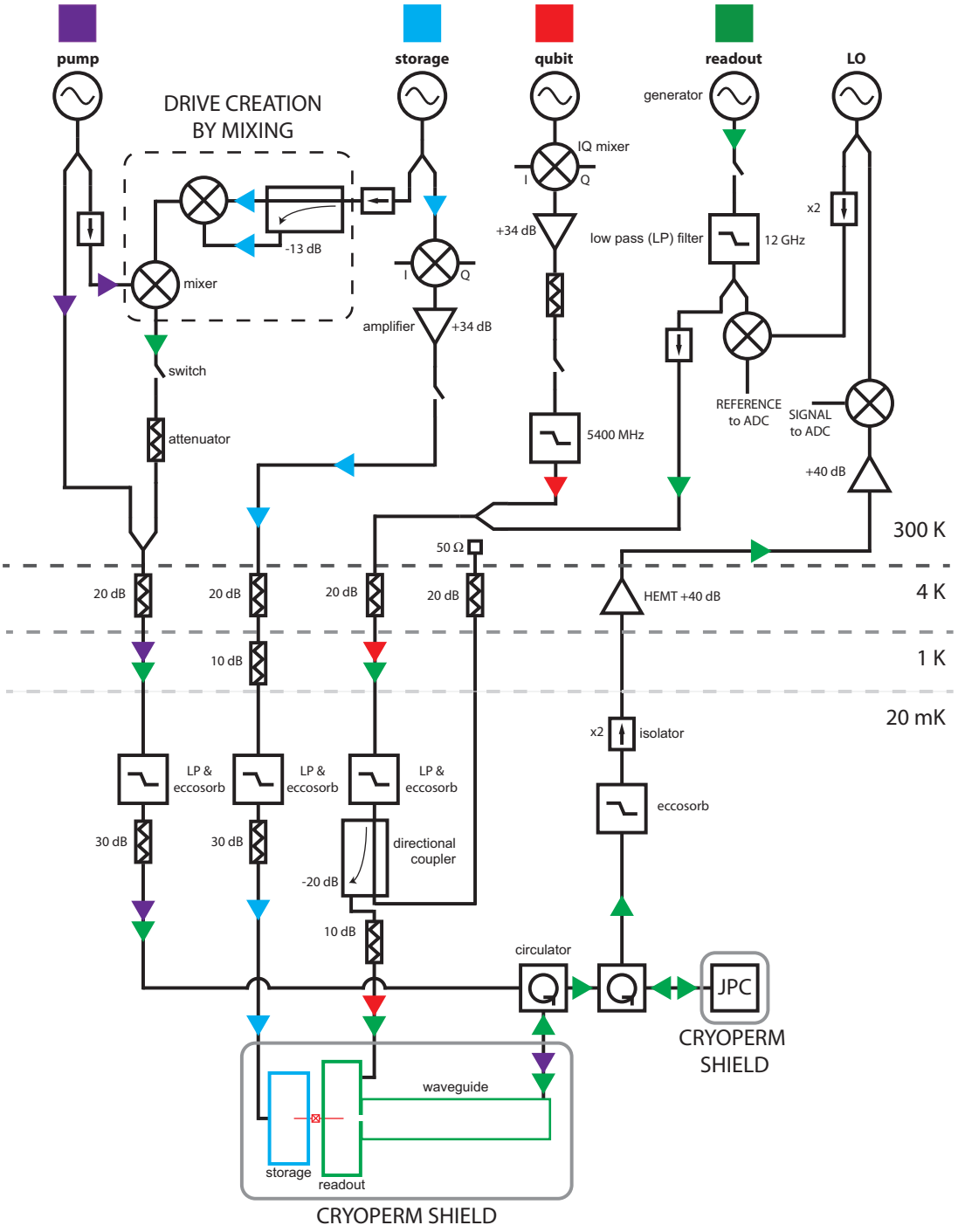

Figure S1: **Experiment schematic.**

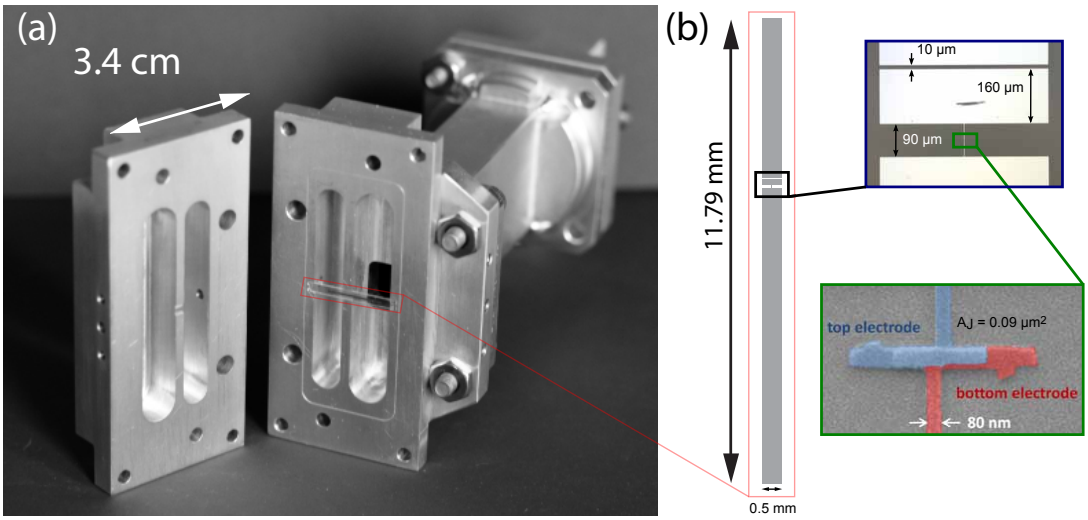

Figure S2: **Pictures of the device.** (a) Photograph of the two halves of the 3D aluminum cavities, the bridge transmon on a sapphire chip, and the rectangular waveguide. The left half is screwed on to the right one. The readout cavity has a hole which couples it to the rectangular waveguide behind it, which in turn is coupled to a transmission line through a waveguide via an SMA adapter. (b) Left : schematics of the Josephson junction (JJ) and the antenna pads. Top right: optical image in the region containing the JJ and the gap capacitor. The visible scratch results from probing the junction resistance. Bottom right: Scanning electron microscope image of the JJ.

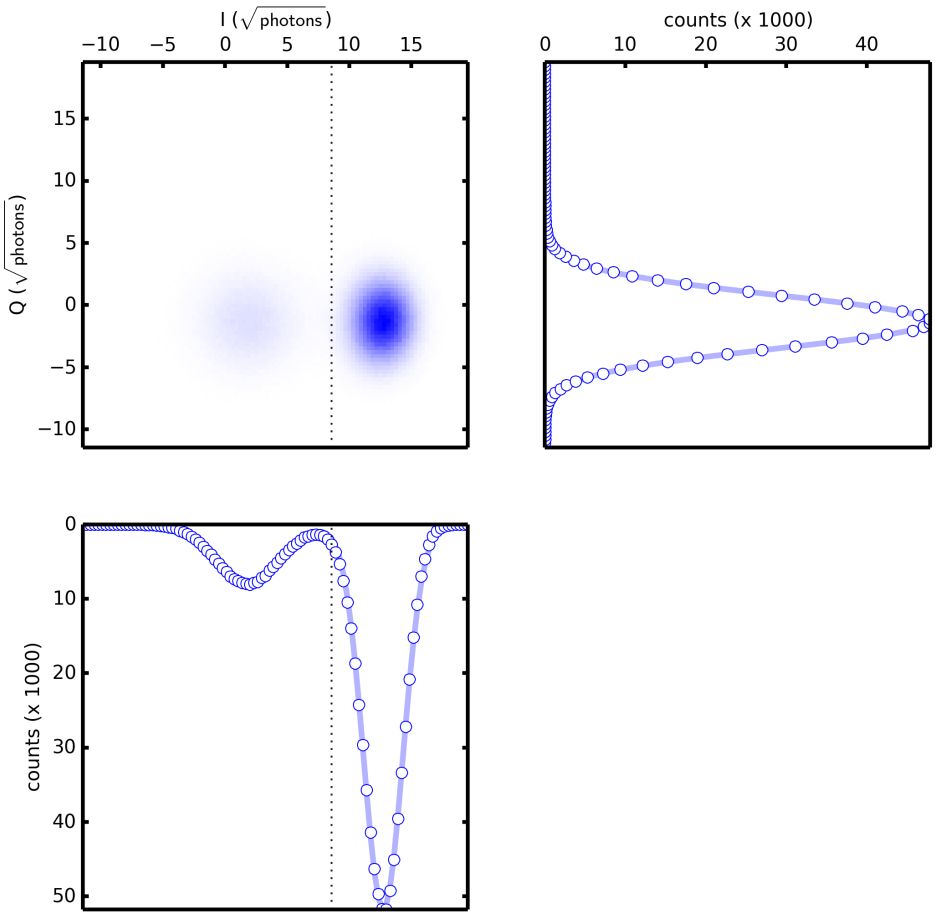

Figure S3: **Single shot readout of the qubit state with the JPC.** Top left panel: two-dimensional histogram of the (I,Q) values of 820,000 measurements of the qubit in thermal equilibrium (20% ground state and 80% excited state). This histogram was rotated such that the information about the qubit state is encoded in the I quadrature. The right and left gaussian distributions correspond to the qubit in $|g\rangle$ and $|e\rangle$ respectively. Bottom panel: histogram of the I values, where the sum of two gaussians (full line) is fitted to the data (full dots). Right panel: Histogram of the Q values, where a single gaussian (full line) is fitted to the data (full dots). The dotted line is the measurement threshold: if a data point lies on the left or right of this threshold, the outcome is associated with $|e\rangle$ or $|g\rangle$ respectively. The gaussian on the right is squeezed in the I quadrature due to the amplifier saturation.

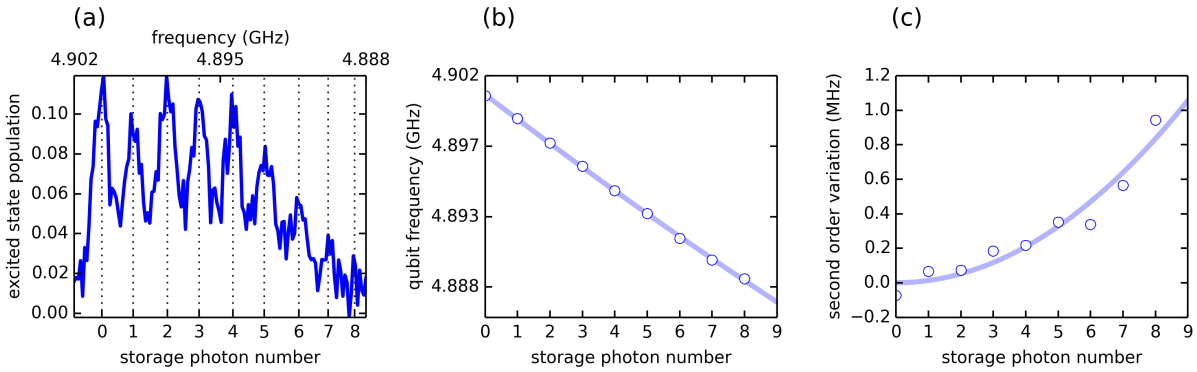

Figure S4: **Qubit frequency as a function of the number of photons in the storage cavity.** When there are n=0 photons in the storage, the qubit frequency is $f_q = 4.9007$ GHz. As we introduce exactly n photons in the storage, the qubit frequency shifts in discrete steps to $f_n = f_q - \frac{\chi_{rq}}{2\pi}n + \frac{\chi_{rq}^{(3)}}{2\pi}n^2$. We fit the data (full dots) to a quadratic function of n (full line), which gives the quantities $\chi_{qr}/2\pi = 1.585$ MHz, and $\chi_{rq}^{(3)}/2\pi = 5$ kHz (*28*). This qubit spectroscopy experiment was performed after the storage reached the statistical mixture of $\pm\alpha_\infty$ after 19 μs of pumping (see last panel of Fig. S11(a)).

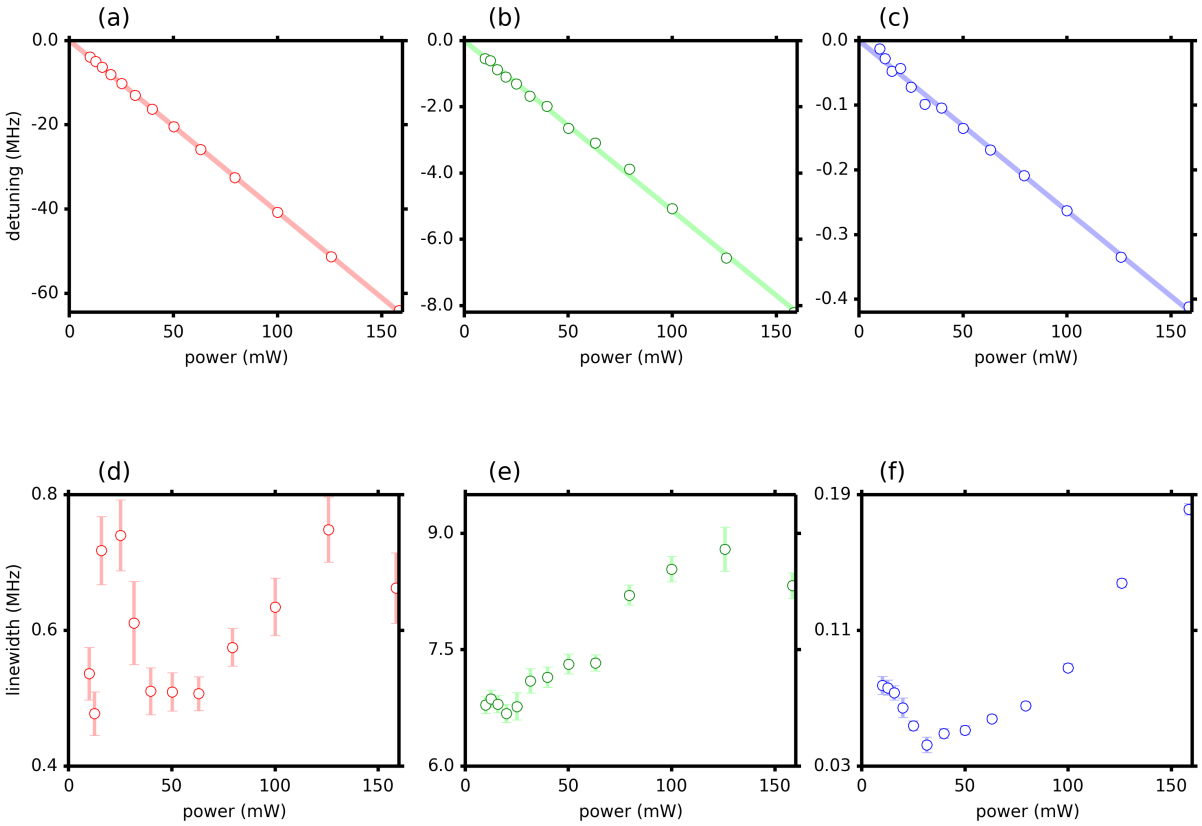

Figure S5: **AC stark shift due to the pump tone.** We place the pump tone at $\omega_p = 8.011$ GHz, and vary its power. For each power, we measure the spectrum of the qubit (a,d), readout mode (b,c) and storage mode (c,e). The frequencies of these modes (a-c) decrease linearly with the pump power, as shown by the linear fit (full line) to the data (full dots). The linewidths are represented in panels (d-f).

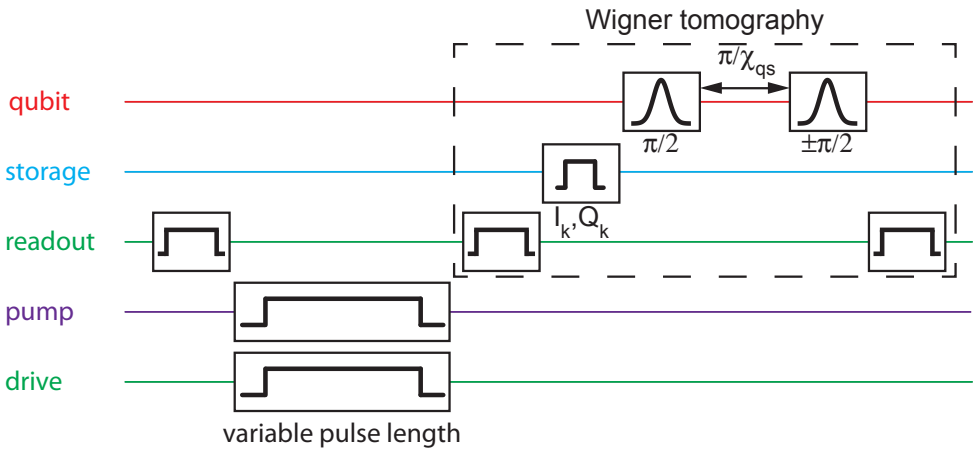

Figure S6: **Pulse sequence which generates the data of Fig. S7.** We first initialize the qubit state by measurement and post-selection. Then we switch on the pump and drive for a variable amount of time. Finally, we perform Wigner tomography. The pulse sequence corresponding to the tomography is in the dashed rectangle and is described in Section 1.4.8.

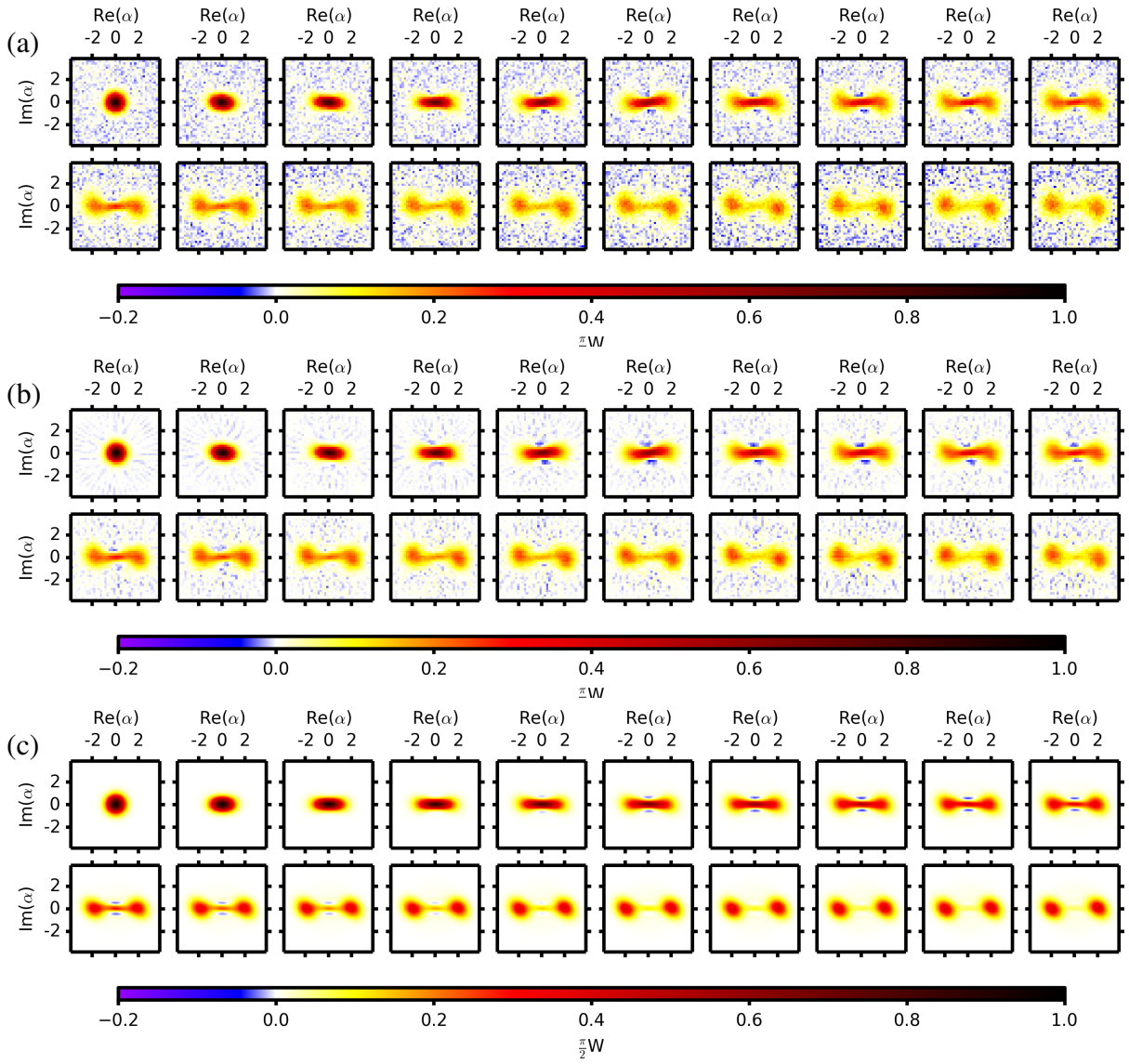

Figure S7: **Evolution of the storage mode state during pumping.** We initialize the storage state in vacuum and switch on the pump and drive tones for various times t_k. Each one of the 20 panels in (a-d), ordered from left to right and top the bottom, is the Wigner function of the storage state after $t_k = k$ μs of pumping. We compare the raw data (a) to the Wigner functions obtained from (b) reconstructed density matrix (*22*) and from (c) numerical simulations. The strong resemblance between the raw data and the Wigner from reconstructions shows that our data can indeed be reproduced by a physically allowed density matrix: that is a positive, hermitian and trace one matrix. This shows that any systematic errors are reasonably low. The numerical simulations are obtained from solving the Lindblad master equation with Hamiltonian Eq. S1, assuming the drive and pump tones have well tuned frequencies, i.e. $\mathbf{H}_{\text{shift}} = 0$. We include photon loss and thermal processes for all three modes. All parameters included in this simulation were independently measured or estimated.

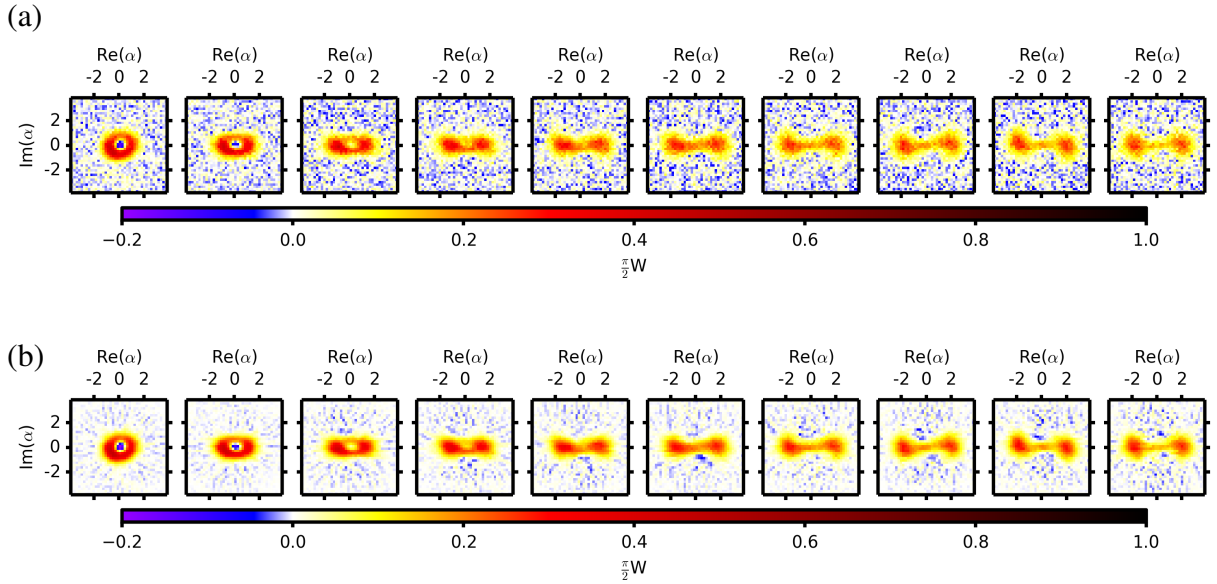

Figure S8: **Evolution of the storage mode state during pumping.** We initialize the storage state in Fock state $|1\rangle$ and switch on the pump and drive tones for various times t_k. Each one of the 10 panels in (a,b), ordered from left to right, is the Wigner function of the storage state after $t_k = k$ μs of pumping. We compare of the raw data (a) to the Wigner functions obtained from a reconstructed density matrix (b). The Fock state is prepared by displacing the storage mode by a coherent state with an average photon number of 0.5, and then projecting to the odd parity manifold by measurement (*28*). As in Fig. S7, the state starts by being squeezed in the Q quadrature. At $t = 3$ μs, the state resembles an odd Schrödinger cat state where a cut of the Wigner function at $I = 0$ displays fringes. Indeed, since we initialize the storage mode in an odd parity state, its evolution under exchanges of photon pairs conserves parity, and hence the transient superposition state has odd parity. As in Fig. S7, the state finally converges to a classical mixture of the two pointer states centered around $|\pm\alpha_\infty\rangle$.

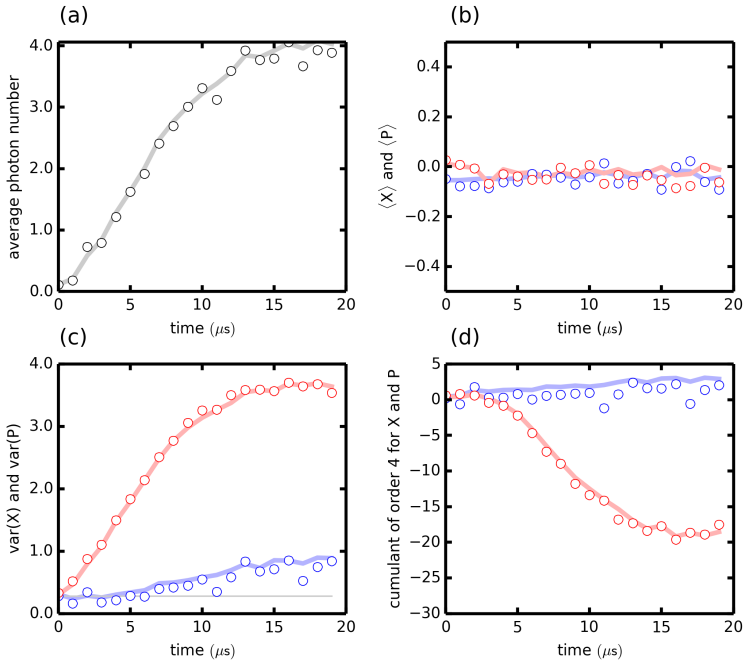

Figure S9: **Expectation values of observables for the storage state during pumping.** From the Wigner functions presented in Fig. S7, we can calculate the expectation value of any observable (*22*). Values extracted from raw data are in full dots, and those extracted from the reconstructed Wigner functions are in full line. We represent the average photon number (a), the averages (b) and the variances (c) of $X = (\mathbf{a}_s + \mathbf{a}_s^\dagger)/2, P = i(\mathbf{a}_s - \mathbf{a}_s^\dagger)/2$. Defining $\bar{X} = X - \langle X \rangle$ and $\bar{P} = P - \langle P \rangle$, we represent in (d) the fourth order cumulants: $\left\langle \bar{X}^4 \right\rangle - 3\left\langle \bar{X}^2 \right\rangle^2$ and $\left\langle \bar{P}^4 \right\rangle - 3\left\langle \bar{P}^2 \right\rangle^2$.

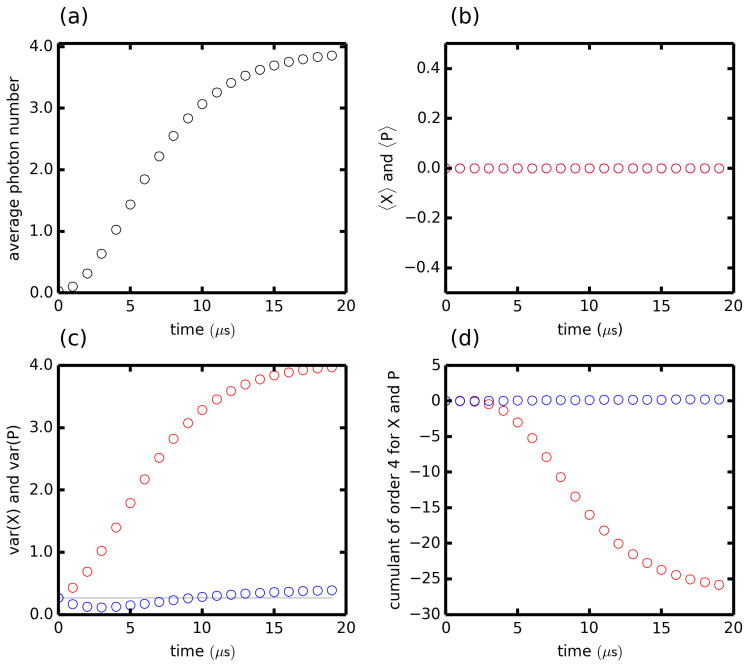

Figure S10: **Expectation values of observables for the storage state during pumping.** Identical description as Fig. S9, where the values are extracted from the numerical simulations described in Fig. S7.

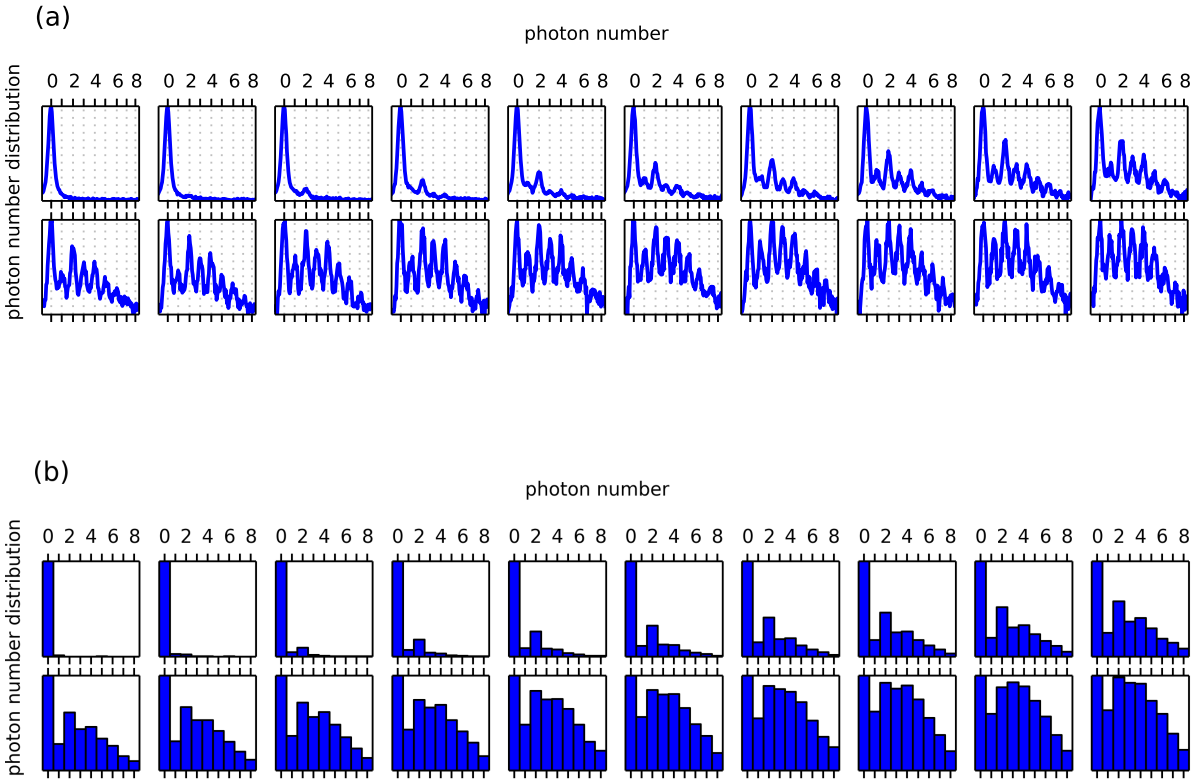

Figure S11: **Photon number distribution of the storage state during pumping.** Each panel k of the 20 panels in (a,b), ordered from left to right and top to bottom, represents the photon number distribution of the storage state after $t_k = k$ μs of pumping. In (a) we perform qubit spectroscopy with a 400 ns sigma gaussian π pulse. Due to the qubit-storage number splitting, this is a measure of the photon number distribution in the storage. In (b), we represent the diagonal of the reconstructed density matrix obtained from the Wigner tomography. These two independent measurements give consistent results, and exhibit the non-poissonian character of the photon number distribution during the transient evolution.

4 Supplementary tables

Mode	Frequency (GHz)	T_1 (μs)	T_2 (μs)	Thermal population
Qubit	4.9007	23	1	20%
Storage	7.57861	20	-	$\leq 5\%$
Readout	7.152	0.025	-	$\leq 2\%$

Table S1: **Frequencies, thermal populations and coherence times of each mode.**

$\chi/2\pi$ (MHz)	Qubit	Storage	Readout
Qubit	130		
Storage	1.585	(0.004)	
Readout	35	0.206	2.14

Table S2: **Dispersive couplings between the qubit, storage and readout modes.** The diagonal elements in this table refer to the self-Kerr terms, which enter in the Hamiltonian as $\sum_{m=q,r,s} -\frac{\chi_{mm}}{2}{\mathbf{a}_m^\dagger}^2\mathbf{a}_m^2$, where the subscripts $m = q, r, s$ stand respectively for the qubit, readout and storage. The off-diagonal terms in the table are the cross-Kerr terms, which enter the Hamiltonian as $-\chi_{qs}\mathbf{a}_q^\dagger\mathbf{a}_q\mathbf{a}_s^\dagger\mathbf{a}_s - \chi_{qr}\mathbf{a}_q^\dagger\mathbf{a}_q\mathbf{a}_r^\dagger\mathbf{a}_r - \chi_{rs}\mathbf{a}_r^\dagger\mathbf{a}_r\mathbf{a}_s^\dagger\mathbf{a}_s$. The value for the storage Kerr (between brackets) was not directly measured, but only estimated from other measured quantities using the geometric equality: $\chi_{ss} = \chi_{qs}^2/4\chi_{qq}$ (*32*).

References and Notes

1. C. Sayrin, I. Dotsenko, X. Zhou, B. Peaudecerf, T. Rybarczyk, S. Gleyzes, P. Rouchon, M. Mirrahimi, H. Amini, M. Brune, J. M. Raimond, S. Haroche, Real-time quantum feedback prepares and stabilizes photon number states. *Nature* **477**, 73–77 (2011). Medline doi:10.1038/nature10376

2. R. Vijay, C. Macklin, D. H. Slichter, S. J. Weber, K. W. Murch, R. Naik, A. N. Korotkov, I. Siddiqi, Stabilizing Rabi oscillations in a superconducting qubit using quantum feedback. *Nature* **490**, 77–80 (2012). Medline doi:10.1038/nature11505

3. D. Ristè, C. C. Bultink, K. W. Lehnert, L. DiCarlo, Feedback control of a solid-state qubit using high-fidelity projective measurement. *Phys. Rev. Lett.* **109**, 240502 (2012). Medline doi:10.1103/PhysRevLett.109.240502

4. P. Campagne-Ibarcq, E. Flurin, N. Roch, D. Darson, P. Morfin, M. Mirrahimi, M. H. Devoret, F. Mallet, B. Huard, Persistent control of a superconducting qubit by stroboscopic measurement and feedback. *Phys. Rev. X* **3**, 021008 (2013).

5. H. Krauter, C. A. Muschik, K. Jensen, W. Wasilewski, J. M. Petersen, J. I. Cirac, E. S. Polzik, Entanglement generated by dissipation and steady state entanglement of two macroscopic objects. *Phys. Rev. Lett.* **107**, 080503 (2011). Medline doi:10.1103/PhysRevLett.107.080503

6. K. W. Murch, U. Vool, D. Zhou, S. J. Weber, S. M. Girvin, I. Siddiqi, Cavity-assisted quantum bath engineering. *Phys. Rev. Lett.* **109**, 183602 (2012). Medline doi:10.1103/PhysRevLett.109.183602

7. S. Shankar, M. Hatridge, Z. Leghtas, K. M. Sliwa, A. Narla, U. Vool, S. M. Girvin, L. Frunzio, M. Mirrahimi, M. H. Devoret, Autonomously stabilized entanglement between two superconducting quantum bits. *Nature* **504**, 419–422 (2013). Medline doi:10.1038/nature12802

8. Y. Lin, J. P. Gaebler, F. Reiter, T. R. Tan, R. Bowler, A. S. Sørensen, D. Leibfried, D. J. Wineland, Dissipative production of a maximally entangled steady state of two quantum bits. *Nature* **504**, 415–418 (2013). Medline doi:10.1038/nature12801

9. M. Wolinsky, H. J. Carmichael, Quantum noise in the parametric oscillator: From squeezed states to coherent-state superpositions. *Phys. Rev. Lett.* **60**, 1836–1839 (1988). Medline doi:10.1103/PhysRevLett.60.1836

10. A. Wallraff, D. I. Schuster, A. Blais, L. Frunzio, R. Huang, J. Majer, S. Kumar, S. M. Girvin, R. J. Schoelkopf, Strong coupling of a single photon to a superconducting qubit using circuit quantum electrodynamics. *Nature* **431**, 162–167 (2004). Medline doi:10.1038/nature02851

11. M. Mirrahimi, Z. Leghtas, V. V. Albert, S. Touzard, R. J. Schoelkopf, L. Jiang, M. H. Devoret, Dynamically protected cat-qubits: A new paradigm for universal quantum computation. *New J. Phys.* **16**, 045014 (2014). doi:10.1088/1367-2630/16/4/045014

12. G. Kirchmair, B. Vlastakis, Z. Leghtas, S. E. Nigg, H. Paik, E. Ginossar, M. Mirrahimi, L. Frunzio, S. M. Girvin, R. J. Schoelkopf, Observation of quantum state collapse and

revival due to the single-photon Kerr effect. *Nature* **495**, 205–209 (2013). Medline doi:10.1038/nature11902

13. J. D. Teufel, T. Donner, D. Li, J. W. Harlow, M. S. Allman, K. Cicak, A. J. Sirois, J. D. Whittaker, K. W. Lehnert, R. W. Simmonds, Sideband cooling of micromechanical motion to the quantum ground state. *Nature* **475**, 359–363 (2011). Medline doi:10.1038/nature10261

14. P. Drummond, Z. Ficek, Eds., *Quantum Squeezing* (Series on Atomic, Optical, and Plasma Physics, Springer, Berlin, 2004).

15. I. Siddiqi, R. Vijay, F. Pierre, C. M. Wilson, M. Metcalfe, C. Rigetti, L. Frunzio, M. H. Devoret, RF-driven Josephson bifurcation amplifier for quantum measurement. *Phys. Rev. Lett.* **93**, 207002 (2004). Medline doi:10.1103/PhysRevLett.93.207002

16. M. A. Castellanos-Beltran, K. D. Irwin, G. C. Hilton, L. R. Vale, K. W. Lehnert, Amplification and squeezing of quantum noise with a tunable Josephson metamaterial. *Nat. Phys.* **4**, 929–931 (2008). doi:10.1038/nphys1090

17. See the supplementary materials on *Science* Online for details.

18. H. J. Carmichael, *Statistical Methods in Quantum Optics 2* (Series on Theoretical and Mathematical Physics, Springer, Berlin, 2008).

19. B. Johnson, M. D. Reed, A. A. Houck, D. I. Schuster, L. S. Bishop, E. Ginossar, J. M. Gambetta, L. DiCarlo, L. Frunzio, S. M. Girvin, R. J. Schoelkopf, Quantum non-demolition detection of single microwave photons in a circuit. *Nat. Phys.* **6**, 663–667 (2010). doi:10.1038/nphys1710

20. M. I. Dykman, M. A. Krivoglaz, Fluctuations in nonlinear systems near bifurcations corresponding to the appearance of new stable states. *Physica A* **104**, 480–494 (1980). doi:10.1016/0378-4371(80)90010-2

21. A. Ourjoumtsev, H. Jeong, R. Tualle-Brouri, P. Grangier, Generation of optical ‘Schrödinger cats’ from photon number states. *Nature* **448**, 784–786 (2007). Medline doi:10.1038/nature06054

22. B. Vlastakis, G. Kirchmair, Z. Leghtas, S. E. Nigg, L. Frunzio, S. M. Girvin, M. Mirrahimi, M. H. Devoret, R. J. Schoelkopf, Deterministically encoding quantum information using 100-photon Schrödinger cat states. *Science* **342**, 607–610 (2013). Medline doi:10.1126/science.1243289

23. S. Deléglise, I. Dotsenko, C. Sayrin, J. Bernu, M. Brune, J. M. Raimond, S. Haroche, Reconstruction of non-classical cavity field states with snapshots of their decoherence. *Nature* **455**, 510–514 (2008). Medline doi:10.1038/nature07288

24. C. Monroe, D. M. Meekhof, B. E. King, D. J. Wineland, A “Schrödinger cat” superposition state of an atom. *Science* **272**, 1131–1136 (1996). Medline doi:10.1126/science.272.5265.1131

25. M. Hofheinz, H. Wang, M. Ansmann, R. C. Bialczak, E. Lucero, M. Neeley, A. D. O’Connell, D. Sank, J. Wenner, J. M. Martinis, A. N. Cleland, Synthesizing arbitrary quantum states in a superconducting resonator. *Nature* **459**, 546–549 (2009). Medline doi:10.1038/nature08005

26. L. G. Lutterbach, L. Davidovich, Method for direct measurement of the Wigner function in cavity QED and ion traps. *Phys. Rev. Lett.* **78**, 2547–2550 (1997). doi:10.1103/PhysRevLett.78.2547

27. S. Haroche, J.-M. Raimond, *Exploring the Quantum: Atoms, Cavities and Photons* (Oxford Univ. Press, Oxford, 2006).

28. L. Sun, A. Petrenko, Z. Leghtas, B. Vlastakis, G. Kirchmair, K. M. Sliwa, A. Narla, M. Hatridge, S. Shankar, J. Blumoff, L. Frunzio, M. Mirrahimi, M. H. Devoret, R. J. Schoelkopf, Tracking photon jumps with repeated quantum non-demolition parity measurements. *Nature* **511**, 444–448 (2014). Medline doi:10.1038/nature13436

29. D. I. Schuster, A. A. Houck, J. A. Schreier, A. Wallraff, J. M. Gambetta, A. Blais, L. Frunzio, J. Majer, B. Johnson, M. H. Devoret, S. M. Girvin, R. J. Schoelkopf, Resolving photon number states in a superconducting circuit. *Nature* **445**, 515–518 (2007). Medline doi:10.1038/nature05461

30. F. Lecocq, I. M. Pop, Z. Peng, I. Matei, T. Crozes, T. Fournier, C. Naud, W. Guichard, O. Buisson, Junction fabrication by shadow evaporation without a suspended bridge. *Nanotechnology* **22**, 315302 (2011). Medline doi:10.1088/0957-4484/22/31/315302

31. M. Reagor, H. Paik, G. Catelani, L. Sun, C. Axline, E. Holland, I. M. Pop, N. A. Masluk, T. Brecht, L. Frunzio, M. H. Devoret, L. Glazman, R. J. Schoelkopf, Reaching 10 ms single photon lifetimes for superconducting aluminum cavities. *Appl. Phys. Lett.* **102**, 192604 (2013). doi:10.1063/1.4807015

32. S. E. Nigg, H. Paik, B. Vlastakis, G. Kirchmair, S. Shankar, L. Frunzio, M. H. Devoret, R. J. Schoelkopf, S. M. Girvin, Black-box superconducting circuit quantization. *Phys. Rev. Lett.* **108**, 240502 (2012). Medline doi:10.1103/PhysRevLett.108.240502

33. N. Bergeal, F. Schackert, M. Metcalfe, R. Vijay, V. E. Manucharyan, L. Frunzio, D. E. Prober, R. J. Schoelkopf, S. M. Girvin, M. H. Devoret, Phase-preserving amplification near the quantum limit with a Josephson ring modulator. *Nature* **465**, 64–68 (2010). Medline doi:10.1038/nature09035

34. J. Gambetta, A. Blais, D. Schuster, A. Wallraff, L. Frunzio, J. Majer, M. Devoret, S. Girvin, R. Schoelkopf, Qubit-photon interactions in a cavity: Measurement-induced dephasing and number splitting. *Phys. Rev. A* **74**, 042318 (2006). doi:10.1103/PhysRevA.74.042318

35. M. D. Reed, B. R. Johnson, A. A. Houck, L. DiCarlo, J. M. Chow, D. I. Schuster, L. Frunzio, R. J. Schoelkopf, Fast reset and suppressing spontaneous emission of a superconducting qubit. *Appl. Phys. Lett.* **96**, 203110 (2010). doi:10.1063/1.3435463

36. A. P. Sears, A. Petrenko, G. Catelani, L. Sun, H. Paik, G. Kirchmair, L. Frunzio, L. I. Glazman, S. M. Girvin, R. J. Schoelkopf, Photon shot noise dephasing in the strong-dispersive limit of circuit QED. *Phys. Rev. B* **86**, 180504 (2012). doi:10.1103/PhysRevB.86.180504

37. D. H. Slichter, R. Vijay, S. J. Weber, S. Boutin, M. Boissonneault, J. M. Gambetta, A. Blais, I. Siddiqi, Measurement-induced qubit state mixing in circuit QED from up-converted dephasing noise. *Phys. Rev. Lett.* **109**, 153601 (2012). Medline doi:10.1103/PhysRevLett.109.153601